# SARS-CoV-2 S protein ACE2 interaction reveals novel allosteric targets

Palur Raghuvamsi[1]†, Nikhil Tulsian[1,2]†, Firdaus Samsudin[3], Xinlei Qian[4], Kiren Purushotorman[4], Gu Yue[4], Mary Kozma[4], Julien Lescar[5], Peter Bond[1,3]*, Paul MacAry[4]* and Ganesh Anand[1]*

[1] Department of Biological Sciences, National University of Singapore, 14 Science Drive 4, Singapore 117543

[2] Department of Biochemistry, National University of Singapore, 28 Medical Drive, Singapore 117546

[3] Bioinformatics Institute, Agency for Science, Technology, and Research (A*STAR), 30 Biopolis Street, Singapore 138671

[4] Life Sciences Institute, Centre for Life Sciences, National University of Singapore, 28 Medical Drive, Singapore 117546

[5] School of Biological Sciences, National Technological University, 60 Nanyang Drive, Singapore 637551

† These authors contributed equally.

*Correspondence: dbsgsa@nus.edu.sg, micpam@nus.edu.sg, peterjb@bii.a-star.edu.sg

**Running Title:** *Spike-ACE2 interactions allosterically prime proteolytic processing of Spike protein*

**Keywords:** Spike, ACE2, allostery, proteolysis, virus-host interactions, fusion peptide, SARS-CoV-2

25 **Abbreviations:** HDXMS, Hydrogen Deuterium Exchange Mass Spectrometry; MD, molecular

26 dynamics, RFU, Relative Fractional deuterium uptake; RMSF, root mean squared fluctuations;

27 PCA, Principal Component Analysis; S, Spike; UPLC, Ultra Performance Liquid

28 Chromatography;

29

30 **Abstract:** The Spike (S) protein is the main handle for SARS-CoV-2 to enter host cells through

31 surface ACE2 receptors. How ACE2 binding activates proteolysis of S protein is unknown. Here,

32 we have mapped the S:ACE2 interface and uncovered long-range allosteric propagation of ACE2

33 binding to sites critical for viral host entry. Unexpectedly, ACE2 binding enhances dynamics at a

34 distal S1/S2 cleavage site and flanking protease docking site ~27 Å away while dampening

35 dynamics of the stalk hinge (central helix and heptad repeat) regions ~ 130 Å away. This highlights

36 that the stalk and proteolysis sites of the S protein are dynamic hotspots in the pre-fusion state.

37 Our findings provide a mechanistic basis for S:ACE2 complex formation, critical for proteolytic

38 processing and viral-host membrane fusion and highlight protease docking sites flanking the S1/S2

39 cleavage site, fusion peptide and heptad repeat 1 (HR1) as allosterically exposed cryptic hotspots

40 for potential therapeutic development.

41

42 **One Sentence Summary:** SARS-CoV-2 spike protein binding to receptor ACE2 allosterically

43 enhances furin proteolysis at distal S1/S2 cleavage sites

44　　　　The COVID-19 pandemic caused by the SARS-CoV-2 virus has sparked extensive efforts

45　　to map molecular details of its life cycle to drive vaccine and therapeutic discovery.(*1*) SARS-

46　　CoV-2 belongs to the family of *Coronaviridae* which includes other human pathogens including

47　　common cold causing viruses (hCoV-OC43, HKU and 229E), SARS and MERS-CoV.(*2-5*)

48　　SARS-CoV-2 has a ~30 Kbp long positive RNA genome with 14 open reading frames, encoding

49　　4 structural proteins: Spike (S) protein, membrane (M) protein, envelope (E) protein and nucleo-

50　　protein; 16 non-structural proteins and 9 accessory proteins.(*6-8*) An intact SARS-CoV-2 virion

51　　consists of a nucleocapsid core composed of nucleoprotein packaged genomic RNA encapsidated

52　　as a lipid-protein envelope forming a spherical structure of diameter ~100 nm.(*9*) The viral

53　　envelope is decorated with S, M and E proteins.(*9*) The S protein is a club-shaped homotrimeric

54　　class I viral fusion protein that has distinctive 'head' and 'stalk' regions (Fig. 1A).

55　　　　　　A characteristic feature of SARS-CoV-2 is proteolysis of Pre-fusion S protein by host

56　　proteases into S1 and S2 subunits. The S1 subunit comprises an N-terminal domain (NTD) and a

57　　receptor binding domain (RBD) that interacts with the host receptor Angiotensin converting

58　　enzyme-2 (ACE2)(*10, 11*) to initiate viral entry into the host.(*12*) Cryo-electron tomography (cryo-

59　　ET) has been used to capture the distribution and organization of trimeric S protein on the intact

60　　virion,(*9*) revealing that $25 \pm 9$ S protein trimers decorate a single virion with a small percentage

61　　(3%) of embedded S proteins in a post-fusion state adopting an extended helical conformation.

62　　The first virus-host interaction is mediated by the viral S protein with the host ACE2 receptor.(*10*)

63　　Binding to ACE2 primes the S protein for proteolysis at S1/S2 cleavage site into individual S1 and

64　　S2 subunits.(*13, 14*) The S2 subunit is divided into six constituent domains harboring the

65　　membrane fusion machinery of the virus. These comprise the fusion peptide (FP), heptad repeat

66　　(HR1), heptad repeat 2 (HR2), connector domain (CD), transmembrane domain (TM), and

67    cytoplasmic tail (CT).(*15, 16*) Extensive structural studies (*9, 15, 17, 18*) have captured S proteins

68    of coronaviruses in distinct open- (PDB:6VXX)(*15*) and closed- (PDB:6VYB)(*15*) conformational

69    states with regards the RBD, as well as the ectodomain orientation in the pre- and post-fusion

70    states, thereby revealing a high intrinsic metastability of the S protein. The S2 subunit promotes

71    membrane fusion and viral entry (Fig. 1B).

72    Despite extensive cryo-EM studies, how ACE2 binding at the RBD domain primes

73    enhanced proteolytic processing at the S1/S2 site is entirely unknown. Amide hydrogen/deuterium

74    exchange mass spectrometry (HDXMS) is a powerful complementary tool for both virus dynamics

75    (*19*) and mapping protein-protein interactions.(*20*) Here, we describe the dynamics of free S

76    protein, the S:ACE2 complex and describe ACE2 binding-induced allosteric conformational

77    changes across the distal regions of S protein, particularly at the stalk and protease docking sites

78    flanking the S1/S2 cleavage sites. These distal 'hotspots' are critical for the first step of SARS-

79    CoV-2 infection and represent novel targets for therapeutic intervention.

80    **Results and Discussion**

81    **Localizing subunit specific dynamics and domain motions of S protein trimer**

82    Structural snapshots of the ACE2 binding to the SARS-CoV-2 S protein interface have

83    been obtained with the RBD alone.(*10, 16, 21-23*) In this study, we have mapped this interface for

84    the S protein construct (1-1208) with mutations at the S1/S2 cleavage site (PRRAS to PGSAS)

85    and proline substitution at 986-987,(*16*) to block proteolysis during expression and purification

86    (Fig. S1A). The S protein and isolated RBD constructs showed high affinity binding to ACE2 (Fig.

87    S1B). We measured dynamics of a trimer of this near-full length S protein by amide hydrogen-

88    deuterium exchange mass spectrometry (HDXMS). Pepsin proteolysis generated 321 peptides

89    with high signal to noise ratio, accounting for ~87% of the entire S protein (Fig. S2). Glycosylation

4

90    of at least 22 sites have been predicted on S protein.(*24*) Average deuterium exchange at these

91    reporter peptides was monitored for comparative deuterium exchange analysis of S protein, ACE2

92    receptor and S:ACE2 complex, along with a specific ACE2 complex with the isolated RBD. While

93    glycosylation is an important posttranslational modification, our HDXMS study has measured

94    deuterium exchange of non-glycosylated segments of S protein alone. Deuterium exchange (t = 1

95    and 10 min) across all peptides of the free S protein trimer are shown in (Fig. 2). We built an

96    integrative model of the full-length S protein trimer using experimental structures of prefusion S

97    ectodomain in the open conformation (PDB: 6VSB)(*16*) and the HR2 domain from SARS S

98    protein as templates. Mapping the relative deuterium exchange across all peptides onto this S

99    protein model showed the greatest deuterium exchange at the stalk region. (Fig. 2A) This is

100   consistent with earlier studies showing at least 60º sweeping motions of the three identified hinge

101   regions of the stalk.(*18*) This was further verified via all-atom MD simulations of the S protein

102   model embedded in a viral model membrane, which showed significant motions of the S protein

103   ectodomain as a result of the flexible stalk region, (Fig. 2B) as well as large atomic fluctuations

104   around the HR2 domain, compared to the rest of the protein (Fig. S3, Fig. S4).

105        The deuterium exchange heat map showed the highest relative exchange in the S2 subunit

106   (Fig. S3) and helical segments, while peptides spanning the fusion peptide showed relatively lower

107   deuterium exchange. Individually, S1 and S2 subunits showed different intrinsic deuterium

108   exchange kinetics, where the average relative fractional deuterium uptake (RFU) of S1 subunit

109   (~0.25) was lower than the average RFU (~0.35) of S2 subunit (Fig. S3, Table S1). Moreover,

110   peptides connecting the RBD to the remainder of the S protein showed greater deuterium

111   exchange, reflecting its role as a 'hinge' facilitating the RBD populating an ensemble of open- and

112   closed- conformational states (red arrow, Fig. 2C). Indeed, in our simulations of the S protein (Fig.

113    2B), the RBD oriented initially in an 'up'- conformation exhibited spontaneous motion towards

114    the 'down'- conformation relative to the hinge region (Fig. 2D, Fig. S4A). Interestingly, a part of

115    the receptor binding motif, specifically residues 476-486, exhibited a higher degree of flexibility

116    based on its average atomic fluctuations (Fig. 2A, 4C), suggesting that binding to ACE2 receptor

117    would be required to stabilize its motion.

118          The NTD of the S protein showed low overall RFU (~0.2), consistent with its well-

119    structured arrangement of β-sheets connected by loops (Fig. 1B). Importantly, certain regions

120    showed significantly higher deuterium exchange (~0.4), of which two loci (136-143, 243-265)

121    span the dynamic interdomain interactions with the RBD. This is supported by the high per-residue

122    root mean square fluctuations (RMSF) and large principal motions observed for residues 249-259

123    during simulations (Fig. 2C, Fig. S4C). One locus (291-303) at the C-terminal end of the NTD

124    connecting to the RBD showed high deuterium exchange, indicative of relative motions of the two

125    domains. The RBD (Fig. 1D) showed relatively higher deuterium exchange (RFU ~0.35), with the

126    peptides spanning the hinge-regions (318-336) showing greatest deuterium exchange (~0.6).

127    Peptides spanning residues 351-375 and 432-452 showed significantly increased deuterium

128    uptake, and these correspond to the NTD interdomain interaction sites. Interestingly, loci of the

129    RBD implicated in the interface (453-467, 491-510) with ACE2 showed relative higher exchange.

130          Overall, the S2 subunit showed relatively higher RFU than the S1 subunit, with each

131    domain exhibiting specific conformational changes (Fig. 1E, Fig. S4). Peptides spanning the

132    region immediately downstream of the S1/S2 cleavage site showed the highest deuterium uptake

133    (0.6), reflecting the rapid dynamics it undergoes for facilitating cleavage of S protein into two

134    subunits. Congruently, our MD simulations revealed the unstructured loop housing the S1/S2

135    cleavage site (residues 677-689) to be highly dynamic (Figure S4C), with RMSFs reaching >1.0

136   nm. It is important to note that the S1/S2 cleavage site has been abrogated in the construct of the

137   S protein used in this study to block proteolytic processing into S1 and S2 subunits during

138   expression in host cells. We thus observed lower deuterium uptake (and lower RMSF values) at

139   peptides in the central helix and connector domain, suggesting that these act as the central core of

140   prefusion S, while the peptides spanning hinge-segments and heptad repeats (HR1 and HR2)

141   showed high deuterium uptake and RMSF values, indicative of the inherent metastability of S to

142   adopt prefusion, fusion and post-fusion conformations.

143   **Domain-specific and global effects of ACE2 binding to the RBD**

144   Comparative HDXMS analysis of the S protein and S:ACE2 complex revealed large-scale

145   effects upon binding of ACE2. The main target for direct interactions was the RBD. We therefore

146   set out to characterize the effects of ACE2 binding with RBD ('RBD$_S$') present on full S protein

147   (Fig. 4A, 4B) and compared this to an isolated construct of the RBD ('RBD$_{isolated}$') (Fig. 3, Fig.

148   S6). Several peptides of the RBD$_S$ showed decreased exchange upon complexation with ACE2

149   (Fig. 3B). These include peptides 340-359, 400-420, 432-452 and 487-502 in the RBD$_S$:ACE2

150   complex (Fig. 4). These sites are consistent with the interface of the SARS-CoV-2 S protein RBD

151   bound to the ACE2 receptor resolved by X-ray crystallography.(*10*) The high-resolution structures

152   showed that the RBD and ACE2 receptor interact via an extensive interface. However, not all

153   peptides at the interface contribute equally to the binding energetics. HDXMS reveals the residues

154   at the core of this interface to be those within peptides spanning residues 340-359, 400-420, 432-

155   452 and 491-510 (Fig. 4A, 4D, Fig. S3). Interestingly, loci showing large-magnitude deuterium

156   exchange correlate to mutational hotspots(*25*).

157   A close-up of RBD$_{isolated}$:ACE2 complex also showed decreased exchange in peptides

158   spanning these regions (Fig. 3). However, the magnitude of decrease in exchange was significantly

159   greater in $RBD_{isolated}$ than in $RBD_S$, indicating the higher flexibility in the full-length S trimer than

160   in free RBD. High resolution structures have identified the RBD interface interacting with ACE2

161   spanning the peptide covering residues 448-501 (Y449, Y453, N487, Y489, G496, T500, G502,

162   Y505, L455, F456, F486, Q493, Q498 and N501) using only the RBD from the S protein.(*23*)

163   Cryo-EM studies have shown that each RBD in the trimeric S protein can adopt an open

164   conformation irrespective of other RBDs, indicating an absence of cooperativity between the three

165   RBDs within a trimer.(*9*) Therefore, we compared the deuterium exchange profiles of $RBD_{isolated}$

166   with $RBD_S$ and observed differences in dynamics imposed by quaternary contacts (Fig. 3A, Fig.

167   3B). Overall, the loci with high and low deuterium exchange profiles were similar when compared

168   between $RBD_{isolated}$ and $RBD_S$, both at the disordered ACE2 receptor binding region as well as the

169   folded region at the N- and C -termini. In solution $RBD_S$ toggles between open- and closed-

170   conformations resulting in an average readout of deuterium exchange measurements.

171   ACE2 binding to $RBD_{isolated}$ and $RBD_S$ resulted in similar effects, where we observed

172   deuterium exchange protection at the peptide regions spanning the known binding interface of

173   RBD. Notably, increased deuterium exchange was observed at the hinge region (Fig. 3C, Fig. S4)

174   indicating allosteric conformational changes, associated with restricting the open- and closed-

175   states interconversion. Therefore, the destabilization/ local unfolding observed at the hinge region

176   as a result of ACE2 binding enables RBD to maintain open conformation. It therefore seems likely

177   that small molecules and biologics targeting the hinge region to lock RBD in the closed state would

178   be of potential high therapeutic value.

179   **ACE2 binding at the RBD is allosterically propagated to the S1/S2 cleavage site and Heptad**

180   **Repeat**

181     Unexpectedly, ACE2 binding at the RBD induced large-scale changes in deuterium

182     exchange in distal regions of the S protein. Some of the peptides in the stalk of S protein showed

183     decreased exchange in the S:ACE2 complex (Fig. 4C, 4D). This indicates that ACE2 receptor

184     interactions stabilized the hinge dynamics. Decreased exchange was also seen in the distal sites in

185     the S2 subunit, localized at the fusion peptide locus and central helix (CH). Interestingly, increased

186     exchange was seen in multiple peptides flanking the S1/S2 cleavage site, HR1 domain and

187     critically at the S1/S2 cleavage sites (Fig. 4D). Even though the construct used in this study has

188     the proteolysis site mutated, it still resulted in increased dynamics at this S1/S2 locus. Furthermore,

189     this region exhibited high RMSF values during simulations. (Fig. S4B). These results clearly

190     indicate that ACE2 binding induces allosteric enhancement of dynamics at this locus, providing

191     mechanistic insights into the conformational switch from the pre-fusion to fusogenic intermediate.

192     Differences in deuterium exchange between free S protein and S:ACE2 complex shows

193     stabilization at ACE2 interacting site and local destabilization at peptides juxtaposed to S1/S2

194     cleavage site (residues 931-938). This suggests that ACE2 binding potentiates peptide of residues

195     931-938 and other high exchanging regions flanking the S1/S2 cleavage site for enhanced furin

196     protease binding and cleavage. Importantly, these results suggest that the S1/S2 cleavage site is a

197     critical hotspot for S protein dynamic transitions for viral entry into the host, and therefore

198     represents a new target for inhibitory therapeutics against the virus.

199     **Dynamics of ACE2 with RBD and S protein provides insights into viral-entry into host**

200     Considering the indispensable role of ACE2 binding in SARS-CoV-2 infection, it is crucial to

201     assess the effects of S protein and RBD binding on ACE2 dynamics. We therefore mapped the

202     corresponding binding sites of RBD, both isolated and within the Spike, on ACE2. The S:ACE2

203     complex represents the prefusion pre-cleavage state wherein full-length S protein is bound to the

9

204    ACE2 receptor (Fig. 1B ii), while the $RBD_{isolated}$:ACE2 complex represents the post-furin cleavage

205    product formed by the S1 subunit and ACE2 (Fig. 1B iii). Previous studies have shown that 14 key

206    amino acids of RBD interact with ACE2, wherein mutations at 6 amino acids resulted in higher

207    binding affinity of SARS-CoV-2.(26) SARS-CoV-2 adopted a different binding mode to ACE2 as

208    a superior strategy for infection in comparison to SARS-CoV-1. A crystal structure of

209    $RBD_{isolated}$:ACE2 complex has identified 24 key ACE2 residues, spanning across peptides 16-45,

210    79-83, 325-330, 350-357 and Arg393.(27) While most of these residues are conserved in binding

211    to both SARS-CoV-1 and SARS-CoV-2, Arg393 and residues 325-330 are unique to SARS-CoV-

212    1 interaction.(25) Interestingly, we observed increased deuterium exchange at these residues in the

213    S:ACE2 complex compared to ACE2 alone (Fig. S8). Identifying the intrinsic dynamics and

214    allosteric changes due to binding could potentially better inform drug development.

215         Simulations of the ACE2 dimer complexed with the $B^0AT1$ amino acid transporter (PDB:

216    6M1D)(12) in a model epithelial membrane revealed a large motion of the peptidase domain (PD),

217    which recognizes the S protein RBD, with respect to the transmembrane and juxtamembrane

218    domains (Fig. S7). This large motion is reminiscent of the flexible tilting displayed by the S protein

219    ectodomain itself, suggesting that both S protein and ACE2 have adaptable hinges that allow for

220    orientational freedom of the domains involved in recognition. To understand how S protein

221    binding affects ACE2 dynamics, we performed HDXMS experiments of monomeric ACE2 alone,

222    S:ACE2 and RBD:ACE2 complexes (Fig. S7, Fig. S8) and mapped the deuterium exchange values

223    on a deletion construct of ACE2 (PDB: 1R42)(27) (Fig. S7, Fig. S8). We observed a reduction in

224    deuterium exchange across both $RBD_{isolate}$:ACE2 and larger S:ACE2 complexes compared to free

225    ACE2 (Figure S8B and S8C). Differences in deuterium exchange between $RBD_{isolated}$:ACE2

226    complex and free ACE2 showed that RBD binding stabilizes ACE2 globally, specifically large

227  differences at the binding site (peptides 21-29, 30-39, and 75-92), and also at distal regions

228  (peptides 121-146, 278-292, 575-586) from RBD binding site of ACE2 (Fig. S8D). Cryo-EM

229  studies have shown that a dimeric full length ACE2 receptor can stably bind to one trimer of the S

230  protein.(*12*)

231  **Conclusions**

232  Here a combination of HDXMS and MD simulations provide a close-up of S protein

233  dynamics in the pre-fusion, ACE2 bound and other associated conformations. Our results reveal

234  the energetics of the S:ACE2 complex interface. ACE2 binding to the isolated RBD and S protein

235  alike lead to binding and stabilization. Interestingly, ACE2 binding to the RBD induces global

236  conformational changes across the entire S protein. Importantly, the stalk region undergoes

237  dampening of conformational motions while causing increased deuterium exchange in the protease

238  sites. Regions highlighting the allosteric propagation of ACE2 binding represent cryptic targets

239  for small molecule inhibitor/antibody development as therapeutics.

324 **Figures**



325
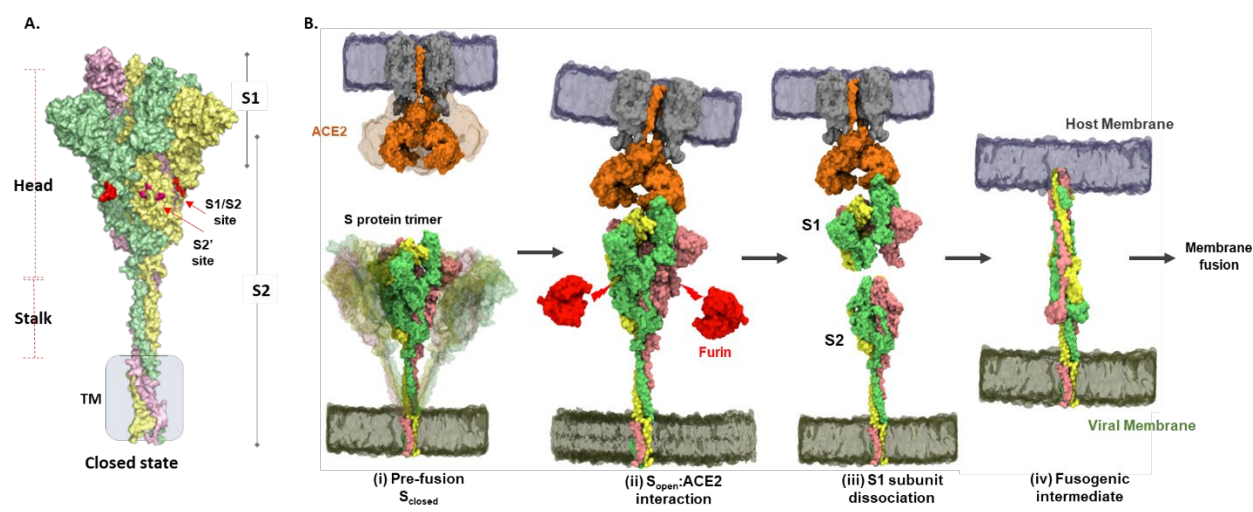
**Figure 1: Structure and domain organization of trimeric S protein showing steps in the virus-host entry initiated by S recognition and binding to ACE2 receptor**

**A.** Prefusion S protein trimer in closed conformational state, with monomers shown in yellow, green and pink. S protein construct (1-1245) used in this study showing head, stalk and transmembrane (TM) segments as generated by integrative modeling. The S1/S2 and S2' cleavage sites are in red. Proteolytic processing (Furin) of S protein generates S1 and S2 subunits. **B**. Schematic of viral entry into host cell mediated by S:ACE2 interactions as previously outlined(*28*): (i) Intrinsic dynamics of pre-fusion S protein trimer decorating SARS-CoV-2 and host ACE2 dimeric structure showing sweeping motions of S protein and ACE2 to facilitate S:ACE2 recognition. (ii) In the open conformation ($S_{open}$), RBD adopts an 'up' orientation to recognize and bind the host membrane-bound ACE2 receptor (PDB: 1R42). ACE2 binding induces conformational changes promoting Furin (red) proteolysis at the S1/S2 cleavage site (red arrows, leading to dissociation of S1 and S2 subunits, mechanism of which is unknown. (iii) The residual ACE2-bound S1 subunit stably bound to ACE2 and S2 subunits dissociate (iv) Conformational

14

340  changes in the separated S2 subunit promote formation of an extended helical fusogenic

341  intermediate (PDB ID: 6M3W),(*17*) for fusion into the host cell membrane, membrane fusion and

342  viral entry into the host cell.(*11*)



343
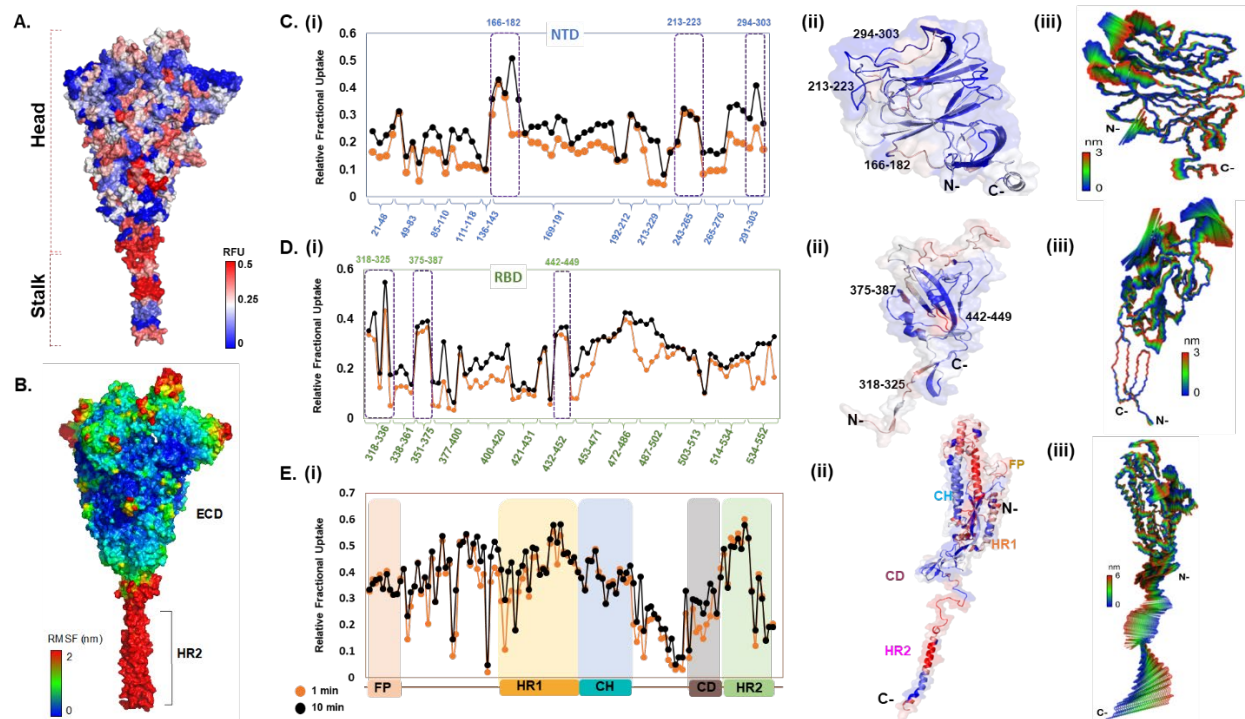
**Figure 2: Deuterium exchange heat map and MD simulations reveal domain-specific conformational dynamics of pre-fusion S protein trimer.**

346  **A.** Deuterium exchange heat map (shades of blue (low exchange) and red (high exchange)) of S

347  protein (residues 1-1208) at t = 1 min deuterium exchange mapped onto structure of S protein. **B.**

348  Per-residue root mean square fluctuations (RMSF) of the S protein (without TM domain) mapped

349  on to the surface of the S trimer. Deuterium exchange based dynamics across N-terminal domain

350  **(C)**, RBD **(D)**, and the S2 subunit **(E)**. (i) Relative fractional deuterium uptake (RFU) plots of

351  NTD, RBD and the S2 subunit at 1 min (orange) and 10 min (black) deuterium exchange times is

352  shown, with pepsin digest fragments displayed from N to C-terminus (X-axis), (see Fig. S2, Table

15

353   S1). (ii) Close-up of the structures of NTD (21-303), RBD (318-552) and the S2 subunit (810-

354   1208). Peptides spanning NTD-RBD interaction sites (166-182, 213-223, 294-303, 318-325, 375-

355   387 and 442-449) showing relatively high deuterium exchange at t-=1 min are highlighted. (iii)

356   The first principal motion and RMSF values of backbone atoms on the NTD, RBD and the S2

357   subunits. Residues with high RMSF are labelled. Different domains (FP, HR1, CH, CD, HR2)

358   showing domain-specific RFU changes are labeled.

359
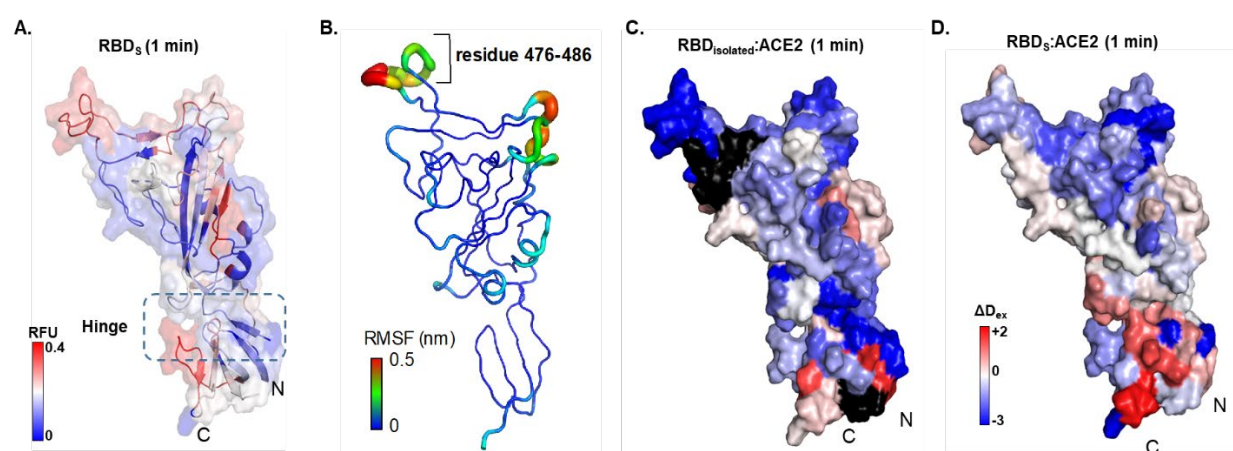


**Figure 3. Map of RBD$_{isolated}$:ACE2 interactions**

**(A)** Relative fractional deuterium uptake values at t = 1 min for RBD (314-547) of S protein (RBD$_S$) mapped on to the structure of RBD extracted from S protein model (see Table S2). High and low exchanging regions are represented as shown in key, and regions with no coverage are shown in black. **(B)** The RMSF values of backbone atoms on the RBD showing residues with high RMSF (476-486), as per key. Differences in deuterium exchanged between RBD$_{isolated}$:ACE2 complex and free RBD$_{isolated}$ **(C)** and RBD$_{spike}$:ACE with free RBD$_{spike}$ **(D)** at 1min of deuterium labelling are mapped on to the structure of RBD. Protection from deuterium uptake and increases in exchange are indicated in blue and red respectively. Regions with no coverage are in black.

16

370
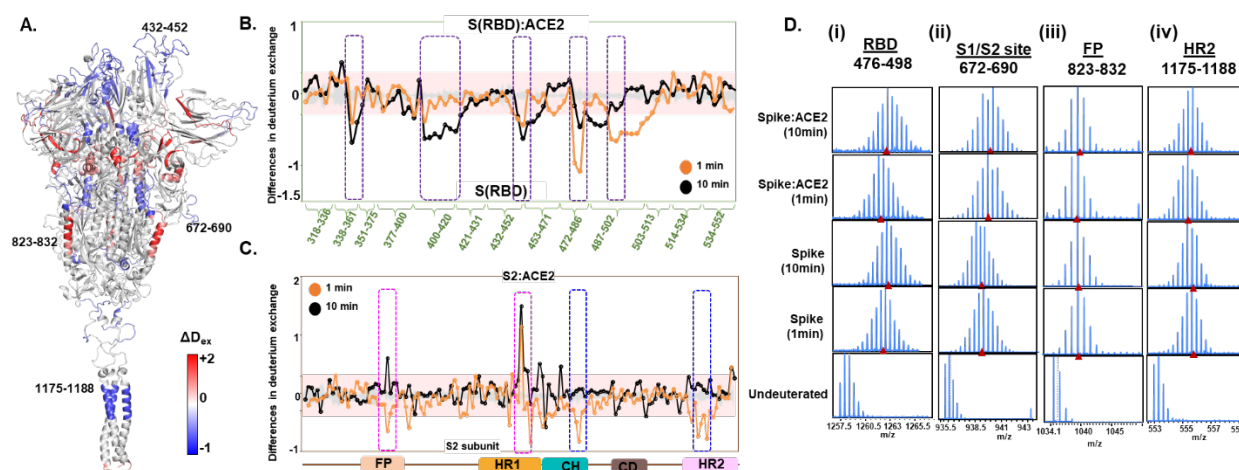
**Figure 4: ACE2 interaction induce large scale allosteric changes across S protein**

**(A)** Differences in deuterium exchange ($\Delta D_{ex}$) (t = 1 min) in S protein upon binding ACE2 showing decreased (blue) and increased (red) deuterium exchange, mapped onto structure of S protein. These differences in deuterium exchange for peptides from **(B)** RBD and S2 subunit **(C)** for pepsin digest fragments (X-axis) are shown. Difference cutoff ±0.3 D is the deuterium exchange significance threshold indicated by pink shaded box with standard error values in gray. Positive differences (>0.3 D) denote increased deuterium exchange and negative differences (<-0.3 D) denote decreased deuterium exchange in S protein bound to ACE2. **(B)** Peptides spanning residues interacting with ACE2 are in purple. **(C)** Peptides spanning fusion peptide (FP) and HR1 are highlighted in pink boxes, while peptides spanning central helix (CH) and heptad repeat 2 (HR2) are in blue. **D.** Stacked mass spectra with isotopic envelopes after deuterium exchange (t = 1, 10 min) for select peptides from (i) RBD (residues 476-498), (ii) S1/S2 cleavage site (residues 672-690), (iii) fusion peptide (residues 823-832) and (iv) HR2 (residues 1175-1188) are shown for the S protein and S:ACE2 complex. Mass spectra of the equivalent undeuterated peptide are shown for reference. The centroid masses are indicated by red arrow-heads.

17

## References

1. N. Bar-Zeev, T. Inglesby, COVID-19 vaccines: early success and remaining challenges. *The Lancet*.

2. V. M. Corman, D. Muth, D. Niemeyer, C. Drosten, Hosts and Sources of Endemic Human Coronaviruses. *Adv Virus Res* **100**, 163-188 (2018).

3. J. R. St-Jean *et al.*, Human respiratory coronavirus OC43: genetic stability and neuroinvasion. *J Virol* **78**, 8824-8834 (2004).

4. S. K. P. Lau *et al.*, Coronavirus HKU1 and other coronavirus infections in Hong Kong. *J Clin Microbiol* **44**, 2063-2071 (2006).

5. S. L. Warnes, Z. R. Little, C. W. Keevil, Human Coronavirus 229E Remains Infectious on Common Touch Surface Materials. *mBio* **6**, e01697-01615 (2015).

6. S. Su *et al.*, Epidemiology, Genetic Recombination, and Pathogenesis of Coronaviruses. *Trends Microbiol* **24**, 490-502 (2016).

7. K. G. Andersen, A. Rambaut, W. I. Lipkin, E. C. Holmes, R. F. Garry, The proximal origin of SARS-CoV-2. *Nat Med* **26**, 450-452 (2020).

8. Y. J. Tan, S. G. Lim, W. Hong, Characterization of viral proteins encoded by the SARS-coronavirus genome. *Antiviral Res* **65**, 69-78 (2005).

9. Z. Ke *et al.*, Structures and distributions of SARS-CoV-2 spike proteins on intact virions. *Nature*, (2020).

10. J. Lan *et al.*, Structure of the SARS-CoV-2 spike receptor-binding domain bound to the ACE2 receptor. *Nature* **581**, 215-220 (2020).

11. M. Hoffmann *et al.*, SARS-CoV-2 Cell Entry Depends on ACE2 and TMPRSS2 and Is Blocked by a Clinically Proven Protease Inhibitor. *Cell* **181**, 271-280.e278 (2020).

12. R. Yan *et al.*, Structural basis for the recognition of SARS-CoV-2 by full-length human ACE2. *Science* **367**, 1444-1448 (2020).

13. A. C. Walls *et al.*, Tectonic conformational changes of a coronavirus spike glycoprotein promote membrane fusion. *Proceedings of the National Academy of Sciences*, 201708727 (2017).

14. N. Vankadari, Structure of Furin Protease Binding to SARS-CoV-2 Spike Glycoprotein and Implications for Potential Targets and Virulence. *The Journal of Physical Chemistry Letters* **11**, 6655-6663 (2020).

15. A. C. Walls *et al.*, Structure, Function, and Antigenicity of the SARS-CoV-2 Spike Glycoprotein. *Cell* **181**, 281-292 e286 (2020).

16. D. Wrapp *et al.*, Cryo-EM structure of the 2019-nCoV spike in the prefusion conformation. *Science* **367**, 1260-1263 (2020).

17. X. Fan, D. Cao, L. Kong, X. Zhang, Cryo-EM analysis of the post-fusion structure of the SARS-CoV spike glycoprotein. *Nat Commun* **11**, 3618 (2020).

18. B. Turonova *et al.*, In situ structural analysis of SARS-CoV-2 spike reveals flexibility mediated by three hinges. *Science*, (2020).

19. X. X. Lim *et al.*, Conformational changes in intact dengue virus reveal serotype-specific expansion. *Nat Commun* **8**, 14339 (2017).

20. X. X. Lim *et al.*, Epitope and Paratope Mapping Reveals Temperature-Dependent Alterations in the Dengue-Antibody Interface. *Structure* **25**, 1391-1402 e1393 (2017).

21. A. Ali, R. Vijayan, Dynamics of the ACE2–SARS-CoV-2/SARS-CoV spike protein interface reveal unique mechanisms. *Scientific Reports* **10**, 14214 (2020).

22. K. K. Chan *et al.*, Engineering human ACE2 to optimize binding to the spike protein of SARS coronavirus 2. *Science* **369**, 1261-1265 (2020).

12

285 23. Q. Wang *et al.*, Structural and Functional Basis of SARS-CoV-2 Entry by Using Human ACE2. *Cell*
286   **181**, 894-904.e899 (2020).
287 24. Y. Watanabe, J. D. Allen, D. Wrapp, J. S. McLellan, M. Crispin, Site-specific glycan analysis of the
288   SARS-CoV-2 spike. *Science* **369**, 330-333 (2020).
289 25. Y. Wang, M. Liu, J. Gao, Enhanced receptor binding of SARS-CoV-2 through networks of hydrogen-
290   bonding and hydrophobic interactions. *Proceedings of the National Academy of Sciences* **117**,
291   13967-13974 (2020).
292 26. F. Li, W. Li, M. Farzan, S. C. Harrison, Structure of SARS coronavirus spike receptor-binding domain
293   complexed with receptor. *Science* **309**, 1864-1868 (2005).
294 27. P. Towler *et al.*, ACE2 X-ray structures reveal a large hinge-bending motion important for inhibitor
295   binding and catalysis. *J Biol Chem* **279**, 17996-18007 (2004).
296 28. J. Shang *et al.*, Structure of mouse coronavirus spike protein complexed with receptor reveals
297   mechanism for viral entry. *PLOS Pathogens* **16**, e1008392 (2020).

298

316

317 **SUPPLEMENTARY MATERIALS**
318 Materials and Methods
319 Figs. S1 to S8
320 Tables S1 to S3
321 References (29-55)

322

323

1

2                 Supplementary Materials for

# SARS-CoV-2 S protein ACE2 interaction reveals novel allosteric targets

5

6   Palur Raghuvamsi[1]†, Nikhil Tulsian[1,2]†, Firdaus Samsudin[3], Xinlei Qian[4],

7   Kiren Purushotorman[4], Gu Yue[4], Mary Kozma[4], Julien Lescar[5], Peter

8   Bond[1,3]*, Paul MacAry[4]* and Ganesh Anand[1]*

9   [1] Department of Biological Sciences, National University of Singapore, 14 Science Drive 4,
10   Singapore 117543
11   [2] Department of Biochemistry, National University of Singapore, 28 Medical Drive, Singapore
12   117546
13   [3] Bioinformatics Institute, Agency for Science, Technology, and Research (A*STAR), 30 Biopolis
14   Street, Singapore 138671
15   [4] Life Sciences Institute, Centre for Life Sciences, National University of Singapore, 28 Medical
16   Drive, Singapore 117546
17   [5] School of Biological Sciences, National Technological University, 60 Nanyang Drive, Singapore
18   637551

19

20   † These authors contributed equally.

21   *Correspondence: dbsgsa@nus.edu.sg, micpam@nus.edu.sg, peterjb@bii.a-star.edu.sg

22

23   **This PDF file includes:**

24
25        Materials and Methods
26        References (29-55)
27        Figs. S1 to S8

28   **Other Supplementary Materials for this manuscript include the following:**

29        Captions for Data S1 to S3

30

## Materials and Methods

<u>Materials</u>

Mass Spectrometry grade acetonitrile, formic acid and water were from Fisher Scientific (Waltham, MA); Deuterium oxide was from Cambridge Isotope Laboratories (Tewksbury, MA). All reagents and chemicals were research grade or higher and obtained from Merck-Sigma-Aldrich (St. Louis, MO).

<u>Methods</u>

**Transient expression and purification of recombinant SARS-CoV2 Spike, RBD and ACE2 receptor**

A near full-length Spike (S) protein, excluding transmembrane domain and cytoplasmic tail, of SARS-CoV-2 (1-1208; Wuhan-Hu-1; GenBank: QHD43416.1) was codon optimized for mammalian cell expression and cloned into pTT5 expression vector (National Research Council Canada, NRCC) with a twin strep tag at the C-terminus (Twist Biosciences). This double mutant Spike construct was generated by mutating RRAR (682-685) into GSAS and residues KV (986-987) into PP. A gene encoding SARS-CoV-2-RBD (319-591 of SARS-CoV-2 Spike) (BioBasic) was cloned into the expression vector pHLmMBP-10 (Addgene) following the N-terminal His and mMBP tag. A gene encoding human ACE2 (residues 21-597; GenBank: AB046569.1) fused to a C-terminal Fc tag (Biobasic) was cloned into vector pHL-sec (Addgene) between the signal peptide and c-terminal His tag. SARS-CoV-2- Spike constructs were expressed in HEK293-6E (NRCC) using polyethylenimine (PEI) as the transfection reagent while the isolated RBD ('RBD$_{isolated}$') and ACE2 constructs were expressed in Expi293F using the Expi293 System (Thermo Fisher). Culture supernatant was harvested on day 7 for HEK293-6E expression and day 5 for Expi293F expression. Spike proteins were affinity purified using Strep-Tactin®XT column (IBA). RBD protein was affinity purified using cOmplete™ His-Tag Purification column (Merck). ACE2 receptor was affinity purified using HiTrap® MabSelect™ SuRe™ column (GE Healthcare). Purified proteins were concentrated and buffer exchanged into PBS using VivaSpin (Sartorius) and the purity was assessed by denaturing polyacrylamide gel electrophoresis (Fig. S1A).

**Deuterium labelling and quench conditions**

Recombinant purified S protein (8 µM), ACE2 receptor (52 µM) and RBD (67 µM) solubilized in phosphate buffer (PBS, pH 7.4) were incubated at 37°C in PBS buffer reconstituted in D$_2$O (99.90%) resulting in a final D$_2$O concentration of 90%. S:ACE2 and RBD:ACE2 complexes (K$_D$ of ~15 nM and ~150 nM, respectively)(*29*) were pre-incubated at 37°C for 30 min in a molar ratio of 1:1 to achieve >90% binding prior to each hydrogen-deuterium exchange reaction. Deuterium labeling was performed for 1 min, 10 min and 100 min for isolated construct of RBD, free ACE2, and RBD$_{isolated}$:ACE2 complex. For isolated S protein and S:ACE2 complex

2

69    1 min and 10 min labelling timescales were used. Pre-chilled quench solution 1.5 M GnHCl and
70    0.25 M Tris(2-carboxyethyl) phosphine-hydrochloride (TCEP-HCl) was added to deuterium
71    exchange reaction mixture to lower the $pH_{read}$ to ~2.5 and lower temperature to ~ 4 °C. Next, the
72    quenched reaction was incubated at 4 °C on ice for 1 min followed by pepsin digestion.

## Mass Spectrometry and peptide identification

74         ~100 pmol quenched samples were injected onto chilled nanoUPLC HDX sample manager
75    (Waters, Milford, MA). The injected samples were subjected to online digestion using
76    immobilized Waters Enzymate BEH pepsin column (2.1 × 30 mm) in 0.1% formic acid in water
77    at 100 μl/min. Simultaneously, the proteolyzed peptides were trapped in a 2.1 × 5 mm C18 trap
78    (ACQUITY BEH C18 VanGuard Pre-column, 1.7 μm, Waters, Milford, MA). Following pepsin
79    digestion, the proteolyzed peptides were eluted using acetonitrile gradient of 8 to 40 % in 0.1 %
80    formic acid at a flow rate of 40 μl $min^{-1}$ into reverse phase column (ACQUITY UPLC BEH C18
81    Column, 1.0 × 100 mm, 1.7 μm, Waters) pumped by nanoACQUITY Binary Solvent Manager
82    (Waters, Milford, MA). Electrospray ionization mode was used to ionize peptides sprayed onto
83    SYNAPT G2-Si mass spectrometer (Waters, Milford, MA) acquired in $HDMS^E$ mode of detection
84    and measurement. A flow rate of 5 μl/min was used to inject 200 fmol $μl^{-1}$ of [Glu[1]]-fibrinopeptide
85    B ([Glu[1]]-Fib) into mass spectrometer for lockspray correction.

86         Undeuterated protein samples were used to identify sequences from mass spectra data (in
87    $HDMS^E$ mode) using Protein Lynx Global Server (PLGS) v3.0. Peptide identification search was
88    performed against a separate sequence database of each protein sequence along with its respective
89    affinity purification tag sequences. In the PLGS search parameters, i) no specific protease and ii)
90    no variable N-linked glycosylation modification options were selected for sequence identification.
91    The identified peptides were further filtered using a minimum intensity cutoff of 2500 for product
92    and precursor ions, minimum products per amino acids of 0.2 and a precursor ion mass tolerance
93    of <10 ppm using DynamX v.3.0 (Waters, Milford, MA) and tested for pepsin cleavage
94    specificity.(*30*) Peptides independently identified under the specified condition and present in at
95    least in two out of three undeuterated samples were retained for HDXMS analysis. S protein
96    contains 22 variable glycosylation sites(*31*) out of which we identified peptides spanning 12
97    glycosylation sites in our sample (Fig. S2). For ACE2, we obtained 4 peptides overlapping the
98    glycosylation sites (Fig S7). Relative fractional deuterium uptake (RFU) is the ratio of number of
99    deuterons exchanged to the total number of exchangeable amides of the peptide. Centroid masses
100   of undeuterated reference spectra were subtracted from equivalent spectra of peptides showing
101   deuterium exchange to calculate the average deuterons exchanged with time for each peptide.
102   Deuterium exchange plots, relative deuterium exchange and difference plots were obtained from
103   DynamX 3.0. N-terminus and prolines were excluded for estimation of exchangeable amides per
104   peptide.(*32*) All deuterium exchange experiments were performed in triplicate and reported values
105   are not corrected for deuterium back exchange.

106

3

**Modelling and molecular dynamics (MD) simulations**

An integrative model of full-length SARS-CoV-2 S protein was built using Modeller v9.21.(*33*) The cryo-EM structure of pre-fusion S ectodomain in the open conformation (PDB: 6VSB)(*29*) was used as the template for the ectodomain (ECD) with missing loops on the NTD modelled based on SARS S NTD crystal structure (PDB: 5X4S).(*34*) The NMR structure of SARS S HR2 domain (PDB: 2FXP)(*35*) was used as the template for the HR2 domain, while the TM domain was modelled using the NMR structure of the HIV-1 gp-41 TM domain (PDB: 5JYN)(*36*). Ten models were built and subjected to stereochemical assessment using the discreet optimized protein energy (DOPE) score(*37*) and Ramachandran analysis.(*38*) The model with the lowest DOPE score and the smallest number of Ramachandran outliers was chosen. Palmitoylation was added to three cysteine residues (C1236, C1240 and C1243) on the CT domain based on a study showing its importance in SARS S protein function.(*39*) The S protein model was then embedded into a model membrane representing the endoplasmic reticulum-Golgi intermediate compartment (ERGIC),(*40*) where coronaviruses are known to assemble in a bud form.(*41, 42*) The ERGIC model membrane was built using CHARMM-GUI Membrane Builder.(*43*) All-atom MD simulation was performed for 200 ns using GROMACS 2018(*44*) and the CHARMM36 force field.(*45*) The systems were solvated with TIP3P water molecules and 0.15 M NaCl salt. Minimization and equilibration were performed following standard CHARMM-GUI protocols.(*46*) Temperature was maintained at 310 K using the Nosé-Hoover thermostat(*47, 48*) and the pressure was maintained at 1 atm using the Parrinello-Rahman barostat.(*49*) Electrostatics were calculated using the smooth particle mesh Ewald (PME) method(*50*) with a real space cut-off of 1.2 nm and the van der Waals were truncated at 1.2 nm with force switch smoothing between 1.0 to 1.2 nm. Constraints were applied to covalent bonds with hydrogen atoms using the LINCS algorithm(*51*) and a 2 fs integration time step was employed. For simulations of the ACE2 receptor, the cryo-EM structure of ACE2-$B^0$AT1 complex in the open conformation (PDB: 6M1D)(*52*) was used. The ACE2-$B^0$AT1 complex was embedded into a model membrane representing the epithelial cell membrane.(*53, 54*) All-atom MD simulation was performed for 200 ns using the protocols described above. Principal component analysis (PCA) and root means square fluctuation (RMSF) analyses were performed using GROMACS, and simulations were visualized in VMD.(*55*)

**Supplementary References**

29. D. Wrapp *et al.*, Cryo-EM structure of the 2019-nCoV spike in the prefusion conformation. *Science* **367**, 1260-1263 (2020).

30. Y. Hamuro, S. J. Coales, K. S. Molnar, S. J. Tuske, J. A. Morrow, Specificity of immobilized porcine pepsin in H/D exchange compatible conditions. *Rapid Commun Mass Spectrom* **22**, 1041-1046 (2008).

31. Y. Watanabe, J. D. Allen, D. Wrapp, J. S. McLellan, M. Crispin, Site-specific glycan analysis of the SARS-CoV-2 spike. *Science* **369**, 330-333 (2020).

32. A. N. Hoofnagle, K. A. Resing, N. G. Ahn, Protein analysis by hydrogen exchange mass spectrometry. *Annu Rev Biophys Biomol Struct* **32**, 1-25 (2003).

33. A. Sali, T. L. Blundell, Comparative protein modelling by satisfaction of spatial restraints. *J Mol Biol* **234**, 779-815 (1993).

34. Y. Yuan *et al.*, Cryo-EM structures of MERS-CoV and SARS-CoV spike glycoproteins reveal the dynamic receptor binding domains. *Nat Commun* **8**, 15092 (2017).

35. S. Hakansson-McReynolds, S. Jiang, L. Rong, M. Caffrey, Solution structure of the severe acute respiratory syndrome-coronavirus heptad repeat 2 domain in the prefusion state. *J Biol Chem* **281**, 11965-11971 (2006).

36. J. Dev *et al.*, Structural basis for membrane anchoring of HIV-1 envelope spike. *Science* **353**, 172-175 (2016).

37. D. Eramian *et al.*, A composite score for predicting errors in protein structure models. *Protein Sci* **15**, 1653-1666 (2006).

38. G. N. Ramachandran, C. Ramakrishnan, V. Sasisekharan, Stereochemistry of polypeptide chain configurations. *J Mol Biol* **7**, 95-99 (1963).

39. C. M. Petit *et al.*, Palmitoylation of the cysteine-rich endodomain of the SARS-coronavirus spike glycoprotein is important for spike-mediated cell fusion. *Virology* **360**, 264-274 (2007).

40. G. van Meer, Lipids of the Golgi membrane. *Trends Cell Biol* **8**, 29-33 (1998).

41. J. Krijnse-Locker, M. Ericsson, P. J. Rottier, G. Griffiths, Characterization of the budding compartment of mouse hepatitis virus: evidence that transport from the RER to the Golgi complex requires only one vesicular transport step. *J Cell Biol* **124**, 55-70 (1994).

42. J. Klumperman *et al.*, Coronavirus M proteins accumulate in the Golgi complex beyond the site of virion budding. *J Virol* **68**, 6523-6534 (1994).

43. J. Lee *et al.*, CHARMM-GUI Membrane Builder for Complex Biological Membrane Simulations with Glycolipids and Lipoglycans. *J Chem Theory Comput* **15**, 775-786 (2019).

44. M. J. Abraham *et al.*, GROMACS: High performance molecular simulations through multi-level parallelism from laptops to supercomputers. *SoftwareX* **1-2**, 19-25 (2015).

45. J. Huang, A. D. MacKerell, Jr., CHARMM36 all-atom additive protein force field: validation based on comparison to NMR data. *J Comput Chem* **34**, 2135-2145 (2013).

46. J. Lee *et al.*, CHARMM-GUI Input Generator for NAMD, GROMACS, AMBER, OpenMM, and CHARMM/OpenMM Simulations Using the CHARMM36 Additive Force Field. *J Chem Theory Comput* **12**, 405-413 (2016).

47. S. Nosé, A molecular dynamics method for simulations in the canonical ensemble. *Molecular Physics* **52**, 255 (1984).

48. W. G. Hoover, Canonical dynamics: Equilibrium phase-space distributions. *Physical Review A* **31**, 1695-1697 (1985).

49. M. Parrinello, A. Rahman, Polymorphic transitions in single crystals: A new molecular dynamics method. *Journal of Applied Physics* **52**, 7182-7190 (1981).

185   50.   U. Essmann *et al.*, A smooth particle mesh Ewald method. *The Journal of Chemical Physics* **103**,
186         8577-8593 (1995).
187   51.   B. Hess, H. Bekker, H. J. C. Berendsen, J. G. E. M. Fraaije, LINCS: A linear constraint solver for
188         molecular simulations. *Journal of Computational Chemistry* **18**, 1463-1472 (1997).
189   52.   R. Yan *et al.*, Structural basis for the recognition of SARS-CoV-2 by full-length human ACE2.
190         *Science* **367**, 1444-1448 (2020).
191   53.   H. P. Jia *et al.*, ACE2 receptor expression and severe acute respiratory syndrome coronavirus
192         infection depend on differentiation of human airway epithelia. *J Virol* **79**, 14614-14621 (2005).
193   54.   J. L. Sampaio *et al.*, Membrane lipidome of an epithelial cell line. *Proc Natl Acad Sci U S A* **108**,
194         1903-1907 (2011).
195   55.   W. Humphrey, A. Dalke, K. Schulten, VMD: visual molecular dynamics. *J Mol Graph* **14**, 33-38,
196         27-38 (1996).

197

198

199 **Supplementary Figures**

200



201
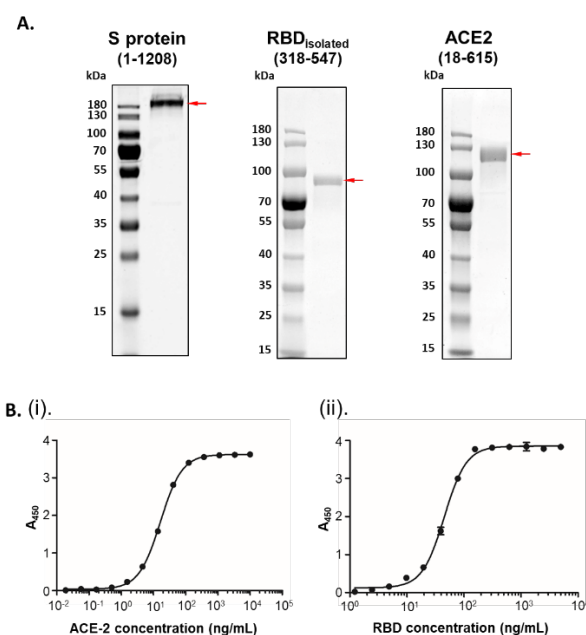
202 **Figure S1:**

203 **Homogeneity of protein samples.** (A) Images of denaturing polyacrylamide gel electrophoresis

204 of purified proteins of the S protein (mutant), isolated RBD and ACE2 are shown, and their

205 molecular sizes are highlighted with red arrow, alongside protein standards. Domain organization

206 is shown for reference. (B) Interactions between ACE2 and RBD represented by the binding

207 curves.

7
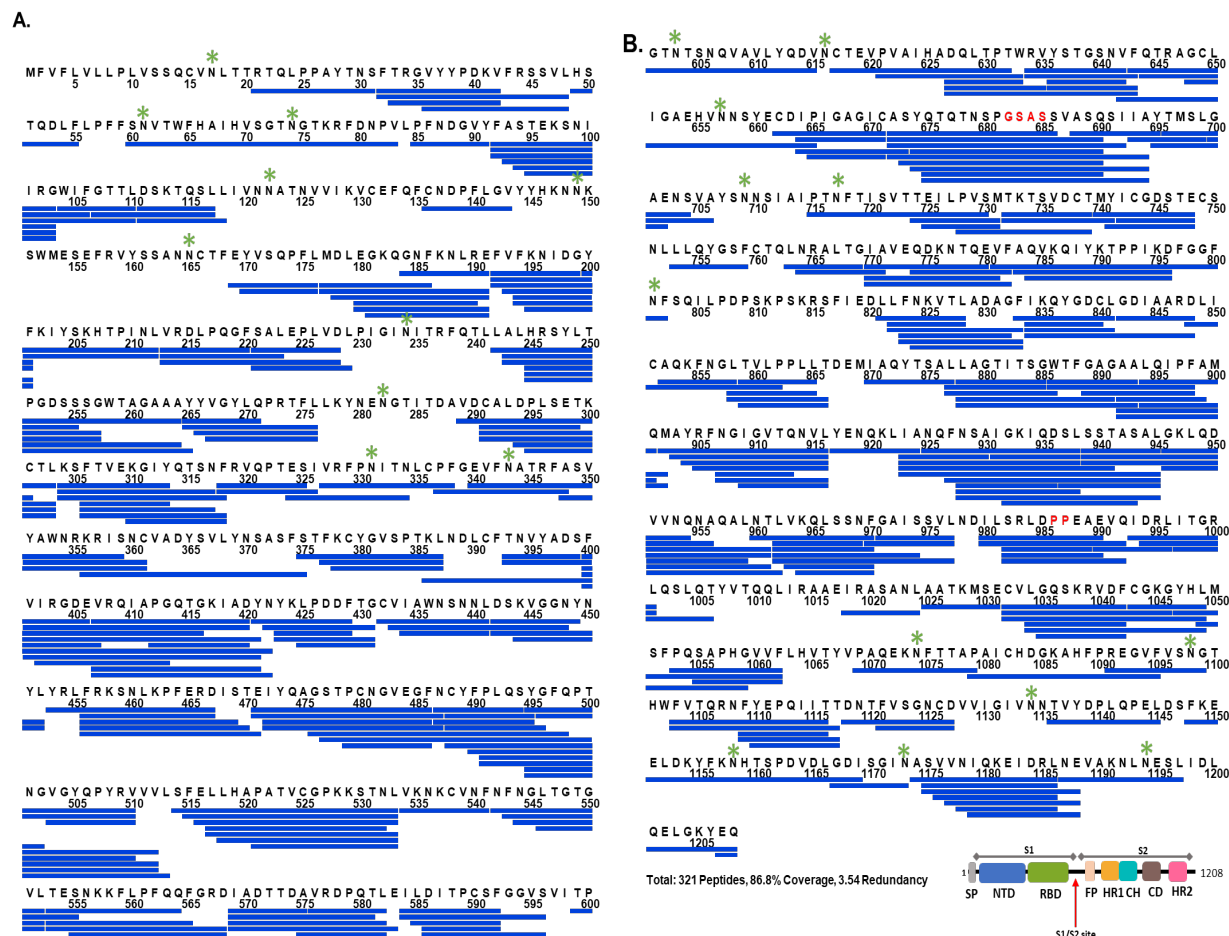
**Figure S2:**

**Primary sequence coverage map of pepsin proteolysed peptides of the S protein.** Coverage map showing 321 peptides spanning 87% of the S protein: (A) 1 – 600 and (B) 601 – 1208, with the mutations highlighted in red. Glycosylation sites are indicated by asterisks (*) and peptide coverage for C-terminal twin strep-tag is not shown. The domain organization for S protein construct 1-1208 is shown.

217
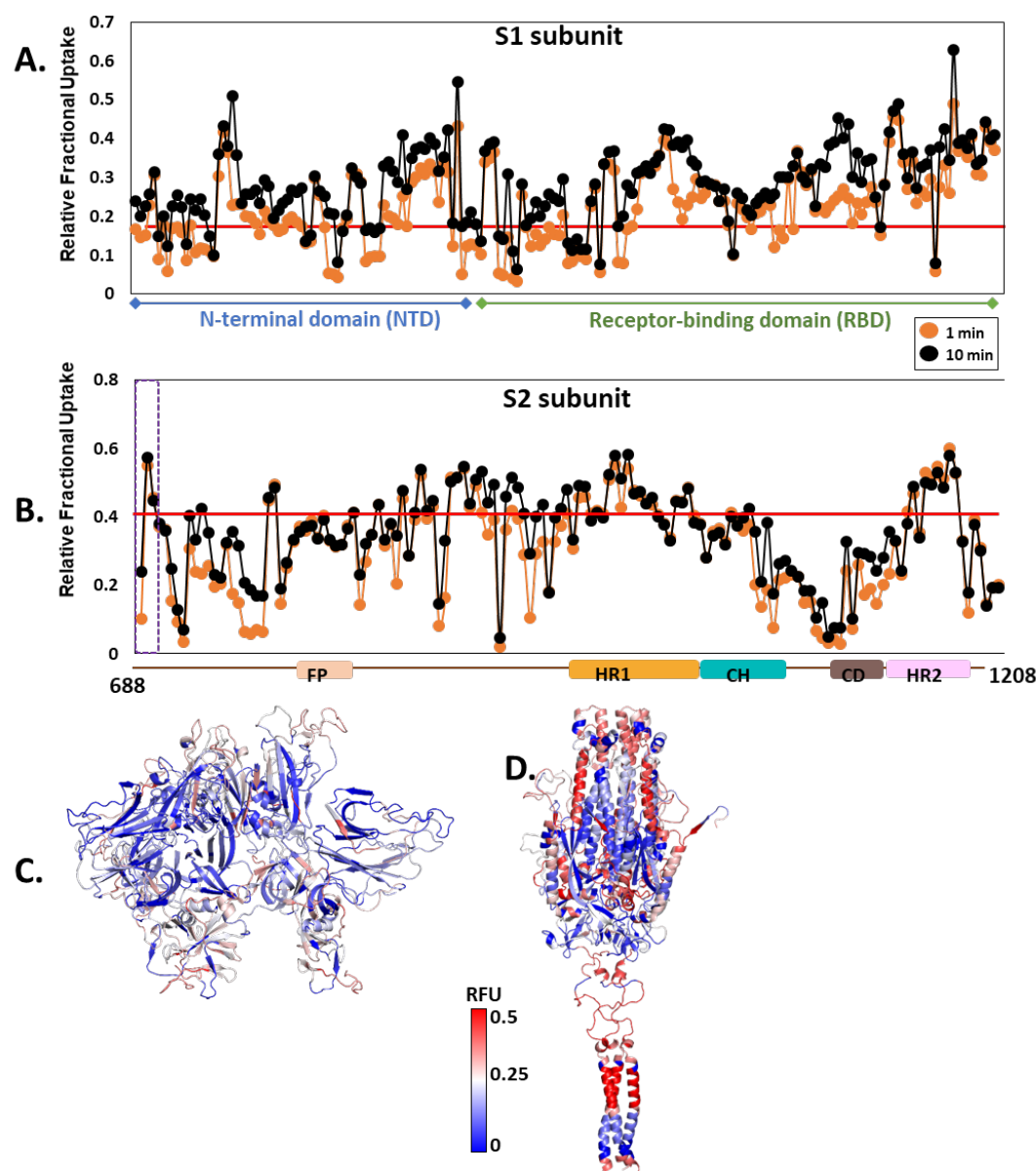
**Figure S3:**

**Time dependent changes in deuterium exchange for free S protein.** Deuterium uptake of each pepsin proteolysed peptide listed from N-to C-terminus (X-axis) spanning S1 subunit (A) and S2 subunit (B) at deuterium labelling times 1 min and 10 min are represented as relative fractional uptake (RFU, Y-axis) values. Red line indicates the average RFU value. RFU values at 1 min of deuterium labelling time mapped on to the structures of the S1 (C) and S2 (D) subunits. High and low exchanging regions are as per key.

225

9

226
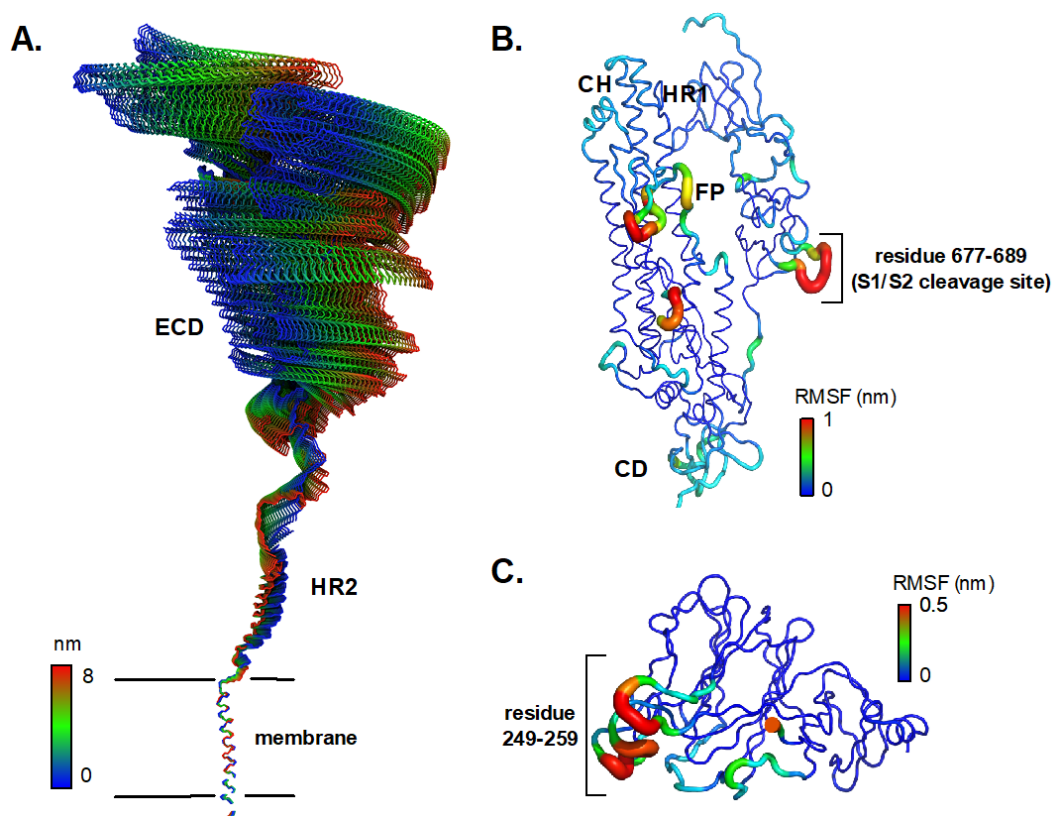
227   **Figure S4:**

228   **Dynamics of the S protein trimer from all-atom MD simulation.** (A) The first principal motion

229   of all backbone atoms for the full-length S protein during all-atom MD simulations as determined

230   by principal component analysis (PCA). (B-C) RMSF values of backbone atoms on the S2 subunits

231   and NTD. Residues with high RMSF are labelled.

10
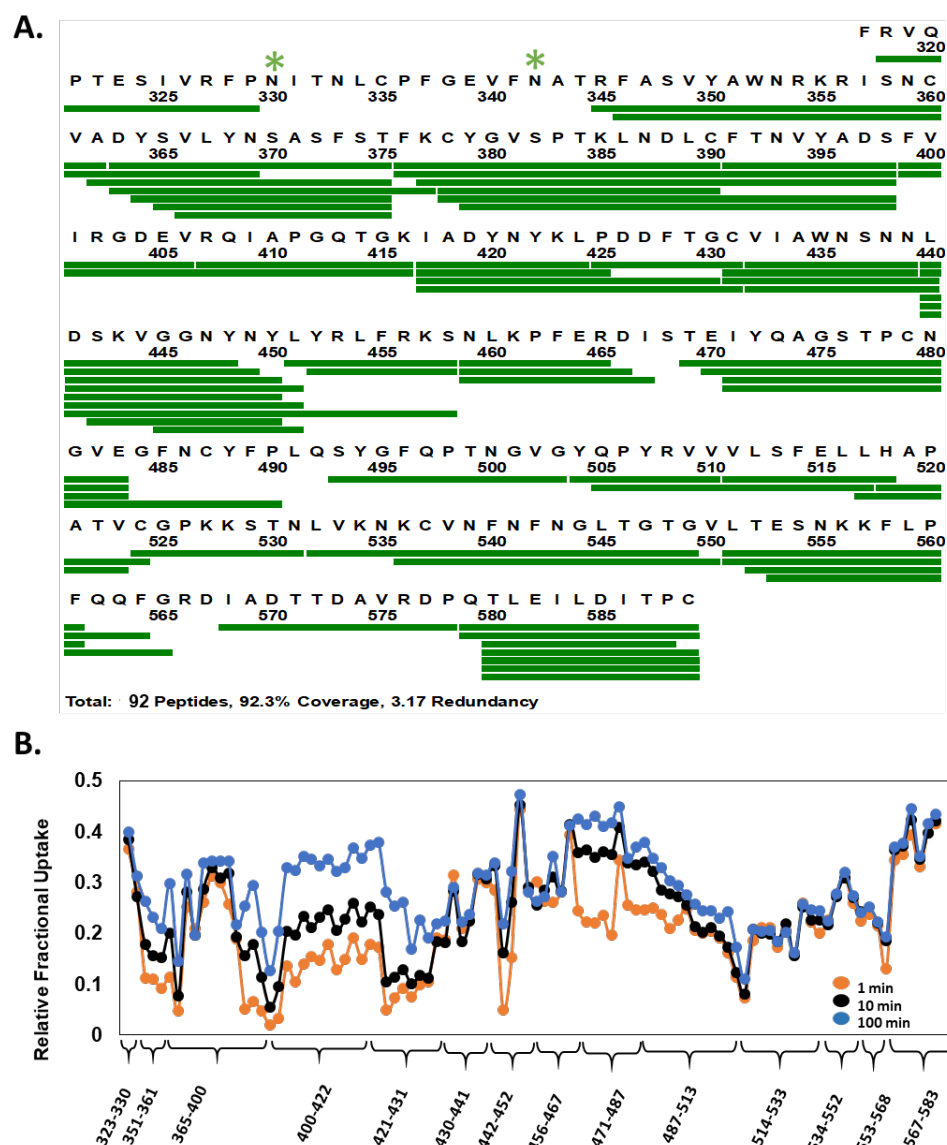
**Figure S5:**

**Primary sequence coverage and deuterium exchange profile of RBD$_{isolated}$ .** (A) Coverage map showing 92 peptides (green bar) spanning ~92% sequence of MBP-RBD$_{isolated}$ (318-589) fusion protein. N-terminal maltose-binding protein (MBP) affinity-tag is not shown. Glycosylation sites are indicated by green asterisk. (B) RFU plot of pepsin proteolyzed peptides of RBD$_{isolated}$ listed N-to C-terminus for deuterium labelling times as per key.

```
                                    S T I E E Q A K T F L D K F N H E A E D L F Y Q S S L A S W N Y
                                      20        25        30        35        40        45        50

      *
    N T N I T E E N V Q N M N N A G D K W S A F L K E Q S T L A Q M Y P L Q E I Q N L T V K L Q L Q A L
        55        60        65        70        75        80        85        90        95       100

      *   *
    Q Q N G S S V L S E D K S K R L N T I L N T M S T I Y S T G K V C N P D N P Q E C L L L E P G L N E
       105       110       115       120       125       130       135       140       145       150

    I M A N S L D Y N E R L W A W E S W R S E V G K Q L R P L Y E E Y V V L K N E M A R A N H Y E D Y G
       155       160       165       170       175       180       185       190       195       200

    D Y W R G D Y E V N G V D G Y D Y S R G Q L I E D V E H T F E E I K P L Y E H L H A Y V R A K L M N
       205       210       215       220       225       230       235       240       245       250

    A Y P S Y I S P I G C L P A H L L G D M W G R F W T N L Y S L T V P F G Q K P N I D V T D A M V D Q
       255       260       265       270       275       280       285       290       295       300

                                      *
    A W D A Q R I F K E A E K F F V S V G L P N M T Q G F W E N S M L T D P G N V Q K A V C H P T A W D
       305       310       315       320       325       330       335       340       345       350

    L G K G D F R I L M C T K V T M D D F L T A H H E M G H I Q Y D M A Y A A Q P F L L R N G A N E G F
       355       360       365       370       375       380       385       390       395       400

                                            *
    H E A V G E I M S L S A A T P K H L K S I G L L S P D F Q E D N E T E I N F L L K Q A L T I V G T L
       405       410       415       420       425       430       435       440       445       450

                                                                                  *
    P F T Y M L E K W R W M V F K G E I P K D Q W M K K W W E M K R E I V G V V E P V P H D E T Y C D P
       455       460       465       470       475       480       485       490       495       500

                                                                                  *
    A S L F H V S N D Y S F I R Y Y T R T L Y Q F Q F Q E A L C Q A A K H E G P L H K C D I S N S T E A
       505       510       515       520       525       530       535       540       545       550

    G Q K L F N M L R L G K S E P W T L A L E N V V G A K N M N V R P L L N Y F E P L F T W L K D Q N K
       555       560       565       570       575       580       585       590       595       600

    N S F V G W S T D W S P Y A D
       605       610       615

    Total: 146 Peptides, 80.2% Coverage, 3.35 Redundancy
```

**Figure S6: Pepsin digest map and sequence coverage ACE2.**

(A) Coverage map showing 140 peptides (pink horizontal bars) covering ~80% sequence of ACE2 (18-615). Sequence of FC-tag is not shown. Glycosylation sites are represented by green asterisk.

12
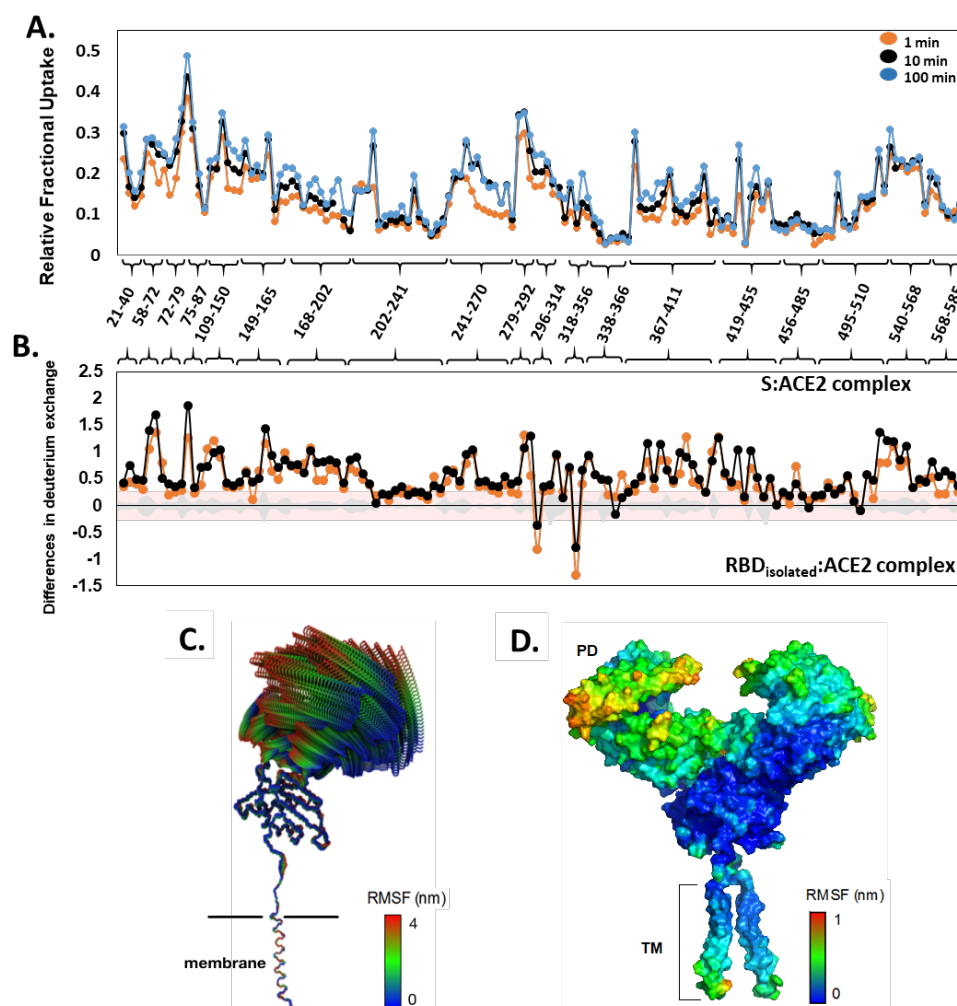
**Figure S7: Deuterium uptake profile for ACE2 receptor and all-atom MD simulation of the ACE2-B0AT1 complex.**

(A) RFU values of pepsin proteolysed peptides listed in N-to C-terminus of ACE2 (peptide 18-615) for deuterium labelling times are shown. (B) Differences in deuterium exchange (Y-axis) of ACE2 peptides listed from N-to C-terminus (X-axis) between S:ACE2 complex and RBDisolated:ACE2 complex. Deuterium exchange significance threshold of ±0.3 D is indicated in red and standard errors in gray. (C) The first principal motion of the all backbone atoms of the ACE2 monomer as determined by PCA. (D) The RMSF values of the ACE2 receptor mapped onto the surface of the ACE2.
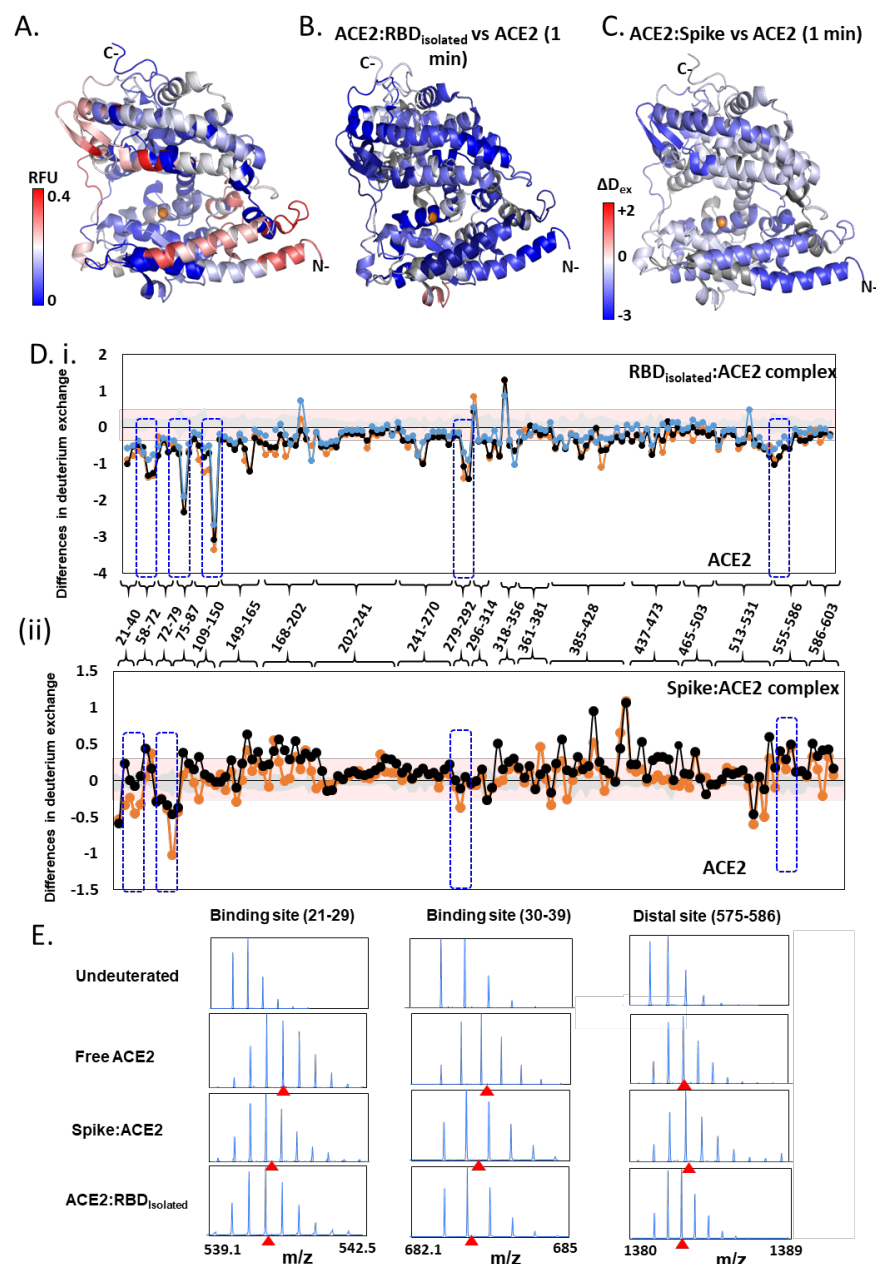
**Figure S8: Effect of RBD_isolated and RBDs complexes on ACE2 dynamics.**

(A) Structure of extracellular domain of ACE2 receptor (PDB ID: 1R42) depicting the RFU at t = 1 min. (B) Differences in deuterium exchange of RBD_isolated:ACE2 complex and free ACE2 at t = 1 min is mapped onto the structure of ACE2, predominantly showing decreased deuterium exchange in ACE2 (shades of blue). (C) Heat map of differences in deuterium exchange (t = 1 min) of S:ACE2 complex and free ACE2. (D) Plot showing differences in deuterium exchange between ACE2 and complexes with RBD (i) and S (ii) at different labeling times. Pepsin digest fragments are indicated by their residue numbers. Cutoff ±0.3 D is the deuterium exchange significance threshold, indicated by pink shaded box, and standard errors are in gray. Positive

267     differences denote increased deuterium exchange in (i) RBD:ACE2 or (ii) S:ACE2 compared to

268     free ACE2, while negative differences denote decreased deuterium exchange. Peptides spanning

269     the sites of interaction with RBD and two distal sites (278-292, 574-585) are highlighted. (E)

270     Stacked mass spectra showing isotopic distribution for select peptides spanning the binding sites

271     (21-29, 30-39) and a distal allosteric site (575-586) for ACE2, S:ACE2 and RBDisolated:ACE2

272     are shown at 1 min deuterium labeling time. Centroids indicated by red arrow-heads.

273

274     **Data S1 to S3**

275     **Table S1:**

276     Relative Fraction uptake values at various deuterium labeling times for Spike and S:ACE2

277     complex

278

279     **Table S2:**

280     Relative Fractional Uptake values at various deuterium labeling times for free and ACE2-bound

281     RBD (isolated)

282

283     **Table S3:**

284     Relative Fractional Uptake values at various deuterium labeling times for free ACE2 and its

285     complexes with isolated RBD and Spike protein

286